Vol.4, No.6, Page 2209- 2218, 2026 https://doi.org/10.59628/jast.v4i6.2925 ISSN 2958-9568 JAST

SUN PUBLISHER

مجلة جامعة صنعاء للعلوم التطبيقية والتكنولوجيا

Sana'a University Journal of Applied Sciences and Technology

https://journals.su.edu.ye/index.php/jast/

Tuning Structural and Optical Properties of $Co_{0.5}Mn_{0.5-x}Zn_xFe_2O_4$ Nanoferrites via Zn Substitution for Optoelectronic Applications

Yousef A. Alsabah[1], Abdelrahman A. Elbadawi[2], Ibrahim Alsuqia[1], Olfat Humaid[1] and A.A. Al-Muntaser[3*]

[1]**Department of Physics, Faculty of Education and Applied Science, Hajjah University, Hajjah, Yemen,**
[2]**Department of physics, Faculty of Science and Technology, Al Neelain University, Khartoum, Sudan ,**
[3]**Department of Physics, Faculty of Education and Applied Sciences at Arhab, Sana'a University, Sana'a, Yemen.**

*Corresponding author: almuntser2015@gmail.com

Abstract

Ferrite nanoparticles are interesting materials due to their rich and unique physical and chemical properties. They find applications in catalysis, bio-processing, medicine, magnetic recording, adsorption, devices, so nanoferrite materials had been synthesized to produce new alternate substance for reducing the rare or high cost of industrial materials. Therefore,$Co_{0.5}Mn_{0.5-x}Zn_xFe_2O_4$ nanoferrite compositions (x=0,0.1,0.2,0.3,0.4) were successfully synthesized via the citrate-nitrate sol-gel auto-combustion technique. A comprehensive investigation of structural and optical, properties was conducted using X-ray diffraction (XRD), Fourier transform infrared spectroscopy (FTIR), and UV–Vis diffuse reflectance spectroscopy (DRS). XRD analysis confirmed the formation of a single-phase cubic spinel structure with space group Fd-3m, without detectable secondary phases, indicating the successful incorporation of Zn^{2+} and Mn^{2+} ions into the cobalt ferrite lattice. The crystallite size was found to vary between 8.017 and 10.130 nm depending on Zn substitution. Rietveld refinement further verified the structural stability with a lattice parameter of a = 8.370 Å and satisfactory fit (x^2 = 0.15). Microstructural parameters such as dislocation density, microstrain, and stacking fault probability were found to increase with decreasing crystallite size. The FTIR spectroscopy confirmed the formation of spinel ferrite and spectra exhibited characteristic metal–oxygen vibration bands at approximately 585 cm^{-1} and 415 cm^{-1}, corresponding to tetrahedral and octahedral sites of the spinel structure. UV–Vis DRS analysis revealed strong absorption in the UV–visible region, with the optical band gap decreasing from 2.96 to 2.81 eV as the Zn concentration increased, demonstrating tunable electronic properties. The absorption coefficient, extinction coefficient, imaginary dielectric constant, and optical conductivity increased with Zn substitution, whereas the refractive index and real dielectric constant showed an opposite trend, with a maximum refractive index observed near 2.6 eV (475 nm). The enhanced optical conductivity around 3.6 eV was attributed to interband transitions and charge-transfer processes such as $O^{2-} \rightarrow Fe^{3+}$ and $Fe^{2+} \leftrightarrow Fe^{3+}$. These results demonstrate that Zn substitution effectively tailors the optical response of Co–Mn ferrites, highlighting their potential for optoelectronic and photonic applications.

Article Info

Keywords:
Nanoferrites, Sol-Gel , Spinel Structure, Optical Properties, XRD.

Article History:
Received: 12-March-2026,
Revised: 19-April-2026,
Accepted: 16-May-2026,
Published: 28 Jun 2026.

1. INTRODUCTION

Spinel ferrite nanoparticles (NPs), with the general formula $MFe_2O_4 (M = Co^{2+}, Zn^{2+}, Mn^{2+}, Ni^{2+}, etc.)$, are a fundamental class of useful materials owing to their tunable magnetic, electrical, optical, and catalytic properties [1, 2]. Their cubic crystal structure, featuring tetrahedral (A) and octahedral (B) interstitial sites, enables precise property engineering through cationic replacement, which dominates the superexchange interactions and charge carrier dynamics [2]. This highlights their common application in many life applications [3–5].

The property optimization of ferrites is often achieved through the synthesis of mixed-metal compositions. Doping with non-magnetic Zn^{2+} ions, which favorably occupy tetrahedral (A) sites, can significantly improve net magnetization via reformed A-B super exchange but typically decreases coercivity [3, 6]. Manganese (Mn^{2+}) substitution is remarkably effective in tailoring electrical properties, frequently increasing resistivity and affecting dielectric loss, producing Mn-substituted ferrites for low-loss, high-frequency applications [2, 7, 8]. Accordingly, the quaternary system $Co_{0.5}Mn_{0.5-x}Zn_xFe_2O_4$ presents an advanced platform to balance magnetic anisotropy, saturation magnetization, electrical resistivity, and optical response for advanced multifunctional applications [3, 9].

The choice of synthesis method represents the first step in preparing a successful spinel. A wide spectrum of physical and chemical methods have been employed. Physical methods such as mechanical alloying, pulsed laser deposition (PLD), wet chemical, bottom-up approaches, Co-precipitation, Hydrothermal/solvothermal, Microemulsion technique, and microwave-aided methods are accessible but often yield noticeable particle size distributions and initiate defects or contamination [3].

Among these, the sol-gel auto-combustion technique appears to be an extremely efficient and versatile route owing to its homogeneity and high-purity output [10–12].

Although extensive research has been conducted on binary and ternary ferrites, comprehensive studies on quaternary systems remain incomplete. This work delivers a comprehensive analysis of the structural, optical, and electrical properties of $Co_{0.5}Mn_{0.5-x}Zn_xFe_2O_4$, where (x=0.0, 0.1,0.2, 0.3, 0.4) nanoferrites were synthesized via the citrate-nitrate sol-gel route, and the effect of Mn^{2+} and Zn^{2+} substitutions was studied.

2. MATERIALS AND METHODS

2.1. Synthesis

$Co_{0.5}Mn_{0.5-x}Zn_xFe_2O_4$ nanoparticles series was successfully prepared by the sol gel, using High-purity reagents from Sigma-Aldrich company namely: $Co(NO_3)_2{\cdot}6H_2O$ (99%), $Zn(NO_3)_2{\cdot}6H_2O$ (99%), $Mn(NO_3)_2{\cdot}4H_2O$ (99%), $Fe(NO_3)_3{\cdot}9H_2O$ (99%), and $C_6H_8O_7$ (citric acid, 99.5%). First, the stoichiometric metal nitrates were dissolved in deionized water under magnetic stirring. A citric acid solution (metal ions: citric acid molar ratio = 1:1.5) was added, and the pH was adjusted to ~7 with ammonia to form stable citrate complexes. The solution was heated at 80 ℃ for 1.5 hours to form a viscous gel, then at 180 ℃ until auto-ignition occurred, after that, yielding a fluffy precursor powder. Lastly, the precursor was ground and calcined at 600 ℃ for 4 hours (5 ℃/min heating rate) to obtain the final crystalline powder (Figure 1) as follows:

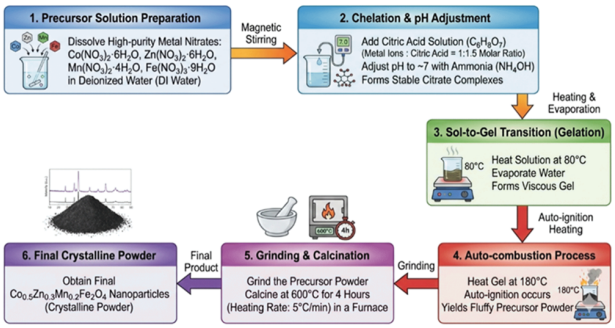

Figure 1. $Co_{0.5}Zn_{0.3}Mn_{0.2}Fe_2O_4$ nanoparticle preparation steps via Sol-gel method.

$$\text{Metal Nitrates}\left(0.5Co^{2+}+(0.5-x)Mn^{2+}+(x)Zn^{2+}+2Fe^{3+}\right)+\text{Citric Acid}\xrightarrow{600\circ C\text{Sol-Gel Combustion}}Co_{0.5}Mn_{(0.5-x)}Zn_xFe_2O_4+\text{Gases}\uparrow(CO_2,N_2,H_2O)$$

2.2. Characterization Techniques

X-ray Diffraction (XRD): The Samples were examined using an X-ray diffractometer (Shimadzu, XRD-7000) [13] operated at 40 kV and a current of 30 mA, and the XRD data of all samples were collected between 10^o and 80^o with a speed of/6 ℃ by s using Cu Kα radiation with λ = 1.5405 Å. The crystallite size was determined from the mean peaks for all samples using Debye–Scherrer's equation Eq. (1) [14, 15] as follows

$$D=\frac{(0.94\lambda)}{(\beta cos\theta)} \quad (1)$$

where D is the crystallite size, λ is the wavelength (1.5405 Å), β is the full width at half maximum, and θ is the diffraction angle. Additionally, the internal strain and the concentration of lattice defects were further analyzed by determining key structural parameters, such as the average dislocation density (δ), microstrain ($\in$), stacking fault probability (SF), and the average inter-separation distance (Y). These values were estimated using the following equations [16]:

$$\delta=\frac{1}{D^2} \quad (2)$$

$$\in=\frac{\beta}{4tan\theta} \quad (3)$$

$$\gamma=\frac{5\lambda}{8sin\theta} \quad (4)$$

$$sf = \left[\frac{2\pi^2}{45(3tan\theta)^2}\right]\beta \quad (5)$$

Fourier Transform Infrared Spectroscopy (FTIR): FTIR data were collected using the KBr pellet method, where the material was mixed with KBr at a ratio of 1:100 for FT-IR measurements between 400 and 2000 cm^{-1}. The chemical groups in the samples were identified using a Fourier transform infrared spectrometer (Satellite FTIR Serial N0 20010102 Voltage. +5/+15/-15 VDC Manufactured in the U.S.A) in the wavelength range of (400-4000) cm^{-1}, [17].

UV-Visible Diffuse Reflectance Spectroscopy (UV-Vis DRS): a ZFQ-9803 Bifurcated Optical Fiber with a fiber diameter of 455 microns, and Ocean Optics for ultraviolet-visible measurement with an integrating sphere recorded data from 200-800 nm with a quartz cuvette. The absorption coefficient calculated for the $Ba_2Zn_{1-x}Ni_xWO_6$ series from the diffuse reflectance data using the Kubelka-Munk function [18]:

$$F(R_\infty) = \frac{\alpha}{s} = \frac{(1-R)^2}{2R} \quad (6)$$

Where $F(R_\infty)$ is the KM function, α is the absorption coefficient, is the scattering coefficient, and R is the reflection coefficient. The Kubelka–Munk function (absorbance) is shown in relation to the wavelength. The absorbance can be used to perceive the absorption edge for band gap energy calculation from the absorption edge according to the relationship, $E_g = \frac{1240}{\lambda}$ (λ is the absorption edge wavelength and represents the band gap) [19], which can also be calculated by [20]:

$$[F(R_\infty)hv]^n = A(h - E_g) \quad (7)$$

Optical Constant Determinations

Optical Constants are important indicators for the samples measured using *UV-Visible* spectroscopy. All measurements were repeated five times for verification and accuracy. From eq (6). In Figure (6), the absorption coefficients are given by $\alpha = sF(R_\infty)$. The refractive index of the sample can be assumed using the following formula [21, 22]:

$$n = \left(\frac{1+R}{1-R}\right) + \sqrt{\left(\frac{4R}{(1-R)^2} - K^2\right)} \quad (8)$$

where k =$(\alpha\lambda/4\pi)$ [23] is the extinction coefficient. The refractive index fluctuates with the variation in the wavelength of the incident light beam.

In addition, the real and imaginary parts of the dielectric constant can be calculated using the following equations:

$$\varepsilon_r = n^2 - k^2 \quad (9)$$

$$\varepsilon_i = 2nk \quad (10)$$

where *k* and *n* are the extinction coefficient and refraction index, respectively. The optical conductivity can be estimated as follows:

$$\sigma_{opt} = (\alpha nc/4\pi) \quad (11)$$

where c is the speed of light. The electrical conductivity (σe) from the optical parameters can be obtained from the following expression [24] :

$$\sigma_e = (2\lambda\sigma_{opt}/\alpha) \quad (12)$$

3. RESULTS AND DISCUSSION

3.1. Structural and Microstructural Analysis

The crystalline structure and phase purity of the synthesized Co-Zn-Mn ferrite nanoparticles were thoroughly investigated using X-ray Diffraction (XRD). Figure (2) shows the XRD patterns of all the prepared nanocomposites ($Co_{0.5}Mn_{0.5}Fe_2O_4$, $Co_{0.5}Zn_{0.1}Mn_{0.4}Fe_2O_4$, $Co_{0.5}Zn_{0.2}Mn_{0.3}Fe_2O_4$, $Co_{0.5}Zn_{0.3}Mn_{0.2}Fe_2O_4$, and $Co_{0.5}Zn_{0.4}Mn_{0.1}Fe_2O_4$). All patterns consistently exhibited characteristic diffraction peaks corresponding to a single-phase cubic spinel structure indexed to the Fd-3m space group. The absence of additional peaks confirmed the high purity of the synthesized materials and the successful incorporation of Zn and Mn ions into the cobalt ferrite lattice without the formation of secondary phases [25].

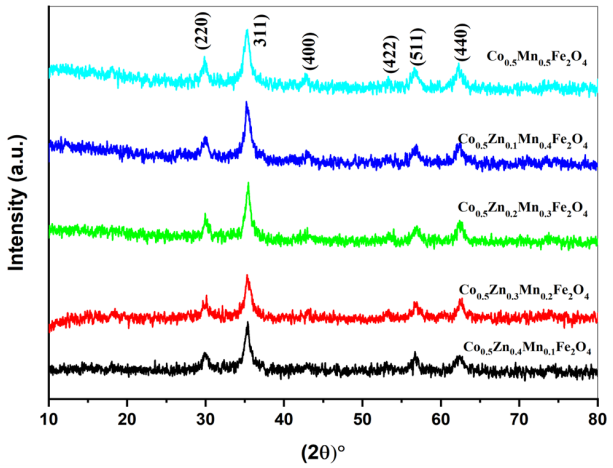

Figure 2. X-ray diffraction pattern of $Co_{0.5}Mn_{0.5-x}Zn_xFe_2O_4$ Nanoparticles prepared series.

A detailed structural analysis was performed using the Fullprof Rietveld refinement method on the XRD data. Figure (3) presents the Rietveld refinement plot for $Co_{0.5}Zn_{0.4}Mn_{0.1}Fe_2O_4$ sample, demonstrating an excellent fit between the experimental and calculated diffraction patterns of the sample. The low chi-squared (x^2)

Table[1]: The Rietveld refinement result of $Co_{0.5}Zn_{0.4}Mn_{0.1}Fe_2O_4$ nanocomposite

$a = b = c = 8.370$ **(Å),** $\alpha = \beta = \gamma = 90°$**,** $\chi^2 = 0.15$

Atomic Position parameters						
Atom	**x**	**y**	**z**	**Occ**	**U**	**Site**
Co	0.00000	0.00000	0.00000	0.500	0.008	16c
Zn	0.00000	0.00000	0.00000	0.400	0.008	16c
Mn	0.00000	0.00000	0.00000	0.100	0.008	16c
Fe	0.62500	0.62500	0.62500	1.060	-0.005	8b
O	0.25000	0.25000	0.25000	1.110	0.007	32e

value of 0.15 for this sample, as indicated in Table (1), underscores the accuracy of the refinement and the validity of the employed structural model. The lattice parameter for $Co_{0.5}Zn_{0.4}Mn_{0.1}Fe_2O_4$ was determined to be a = 8.37000 Å, which is in good agreement with the value of 8.395 Å reported for a similar Co-Zn-Mn ferrite system [26–28]. The result confirmed that the calculated lattice parameter lies between the values stated for $CoFe_2O_4$ (∼8.38 Å) and $ZnFe_2O_4$ (∼8.44 Å) [29] using the FullProf program, confirming the incorporation of larger Zn^{2+} (0.60 Å) and Mn^{2+} (0.66 Å) ions into the lattice compared to Co^{2+} (0.58 Å) [30].

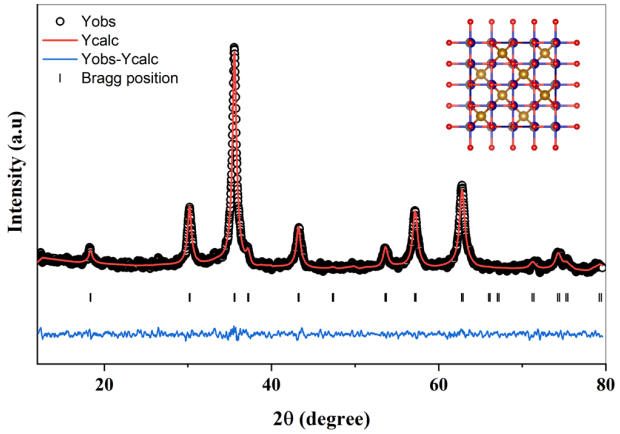

Figure 3. The XRD Retiveld Refinement for the prepared $Co_{0.5}Mn_{0.5-x}Zn_xFe_2O_4$ nanocomposites.

Table (2) shows the microstructural parameters of $Co_{0.5}Zn_xMn_{0.5-x}Fe_2O_4$ Nanoparticles summarizes the crystallite size, dislocation density (δ), microstrain (ε), and stacking fault (SF) for the various Co-Zn-Mn ferrite nanocomposites. The crystallite size found between 8.017 and 10.130 nm was consistent with the other nanoferrites produced via sol-gel auto-combustion and larger crystallite size of the $Co_{0.5}Zn_{0.2}Mn_{0.3}Fe_2O_4$ sample is attributed to the effect of Zn^{2+} ions, which prefer tetrahedral sites, thereby reducing internal stress and lattice distortions at this intermediate concentration. Additionally, the presence of Mn^{2+} (with its large ionic radius) at a proportion of 0.3 helps reduce dislocation density and defects, allowing larger grain growth compared to the other compositions, such as the 25-35 nm range reported for $CoFe_2O_4$ [31, 32].

In addition, this variation in the crystallite size can be influenced by the synthesis conditions and the ionic radii of the substituting elements. The dislocation density (δ), microstrain (ε), and stacking fault (SF) parameters are inversely related to the crystallite size (D). Samples with smaller crystallite sizes, such as $Co_{0.5}Mn_{0.5}Fe_2O_4$ (8.017 nm) and $Co_{0.5}Zn_{0.3}Mn_{0.2}Fe_2O_4$ (8.091 nm), exhibited higher values of δ, ε, and SF. This is consistent with the understanding that smaller crystallites possess a greater proportion of grain boundaries and lattice imperfections, leading to increased internal stress and defect formation. In addition, the constant Y (∼3.17 Å) suggests that the nanoparticle surfaces maintain a fixed separation, likely because of capping agents or electrostatic repulsion, regardless of the internal crystallite dimensions.

Figure (4) shows the FTIR spectrum of the $Co_{0.5}Mn_{(0.5-x)}Zn_xFe_2O_4$ nanoferrite series, which confirms the formation of a single-phase cubic spinel structure, characterized by two primary absorption bands: the high-frequency ν_1 band at approximately 585 cm^{-1} [33], representing the intrinsic stretching vibrations of metal–oxygen (M–O) bonds at the tetrahedral (A) sites, and the low-frequency ν_2 band at 415 cm^{-1}, corresponding to vibrations at the octahedral (B) sites [34]. These positions align perfectly with the established literature for Co–Zn–Mn-substituted ferrites, where the larger ionic radii of Zn^{2+} and Mn^{2+} influence the lattice constant and bond force constants, typically placing these peaks within the 400–600 cm^{-1} range [34, 35].

Beyond the lattice vibrations, the broad absorption at 3430 cm^{-1} and the band at 1630 cm^{-1} indicate O–H stretching and H–O–H bending from surface-adsorbed moisture, while the peak at 1384 cm^{-1} likely stems from residual nitrate (NO_3^-) groups from the synthesis precursors. Ultimately, the presence and sharpness of the ν_1 and ν_2 peaks indicate a high degree of crystallinity and successful incorporation of cobalt, zinc, and manganese into the spinel ferrite lattice [36].

Table[2]: The XRD parameters and energy gap values of $Co_{0.5}Mn_{(0.5-x)}Zn_xFe_2O_4$ series

Sample	Size (nm)	$\delta \times 10^{-3}$ (lines/nm^2)	$\varepsilon \times 10^{-3}$	SF $\times 10^{-3}$	Y (Å)	E_g (eV)
$Co_{0.5}Mn_{0.5}Fe_2O_4$	8.017	15.559	14.240	8.706	3.171	2.96
$Co_{0.5}Zn_{0.1}Mn_{0.4}Fe_2O_4$	8.691	13.238	13.181	8.090	3.182	2.94
$Co_{0.5}Zn_{0.2}Mn_{0.3}Fe_2O_4$	10.130	9.744	11.232	6.842	3.161	2.90
$Co_{0.5}Zn_{0.3}Mn_{0.2}Fe_2O_4$	8.091	15.276	14.125	8.646	3.174	2.85
$Co_{0.5}Zn_{0.4}Mn_{0.1}Fe_2O_4$	9.636	10.769	11.833	7.226	3.167	2.81

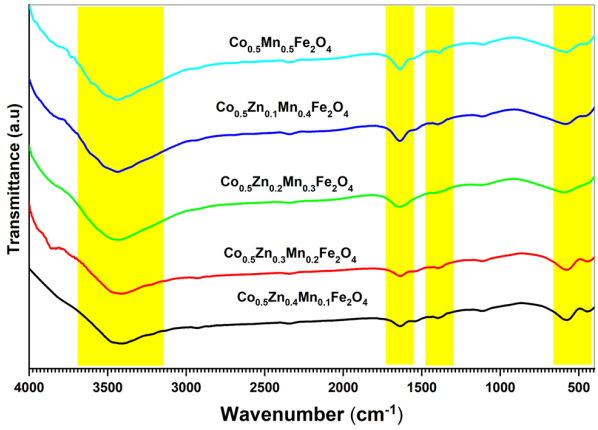

Figure 4. The FTIR spectra for the prepared $Co_{0.5}Mn_{0.5-x}Zn_xFe_2O_4$ nanocomposites.

3.2. Optical Properties Analysis

Figure (5) shows the UV–Vis diffuse reflectance spectra (DRS) of $Co_{0.5}Mn_{0.5-x}Zn_xFe_2O_4$ Nanoparticle Series. All samples exhibited strong absorption in the near-UV and visible regions, with a pronounced absorption edge located between approximately 350 and 450 nm and a broad absorption tail extending up to 800 nm. This behavior is characteristic of spinel ferrites such as $CoFe_2O_4$, $MnFe_2O_4$, and $ZnFe_2O_4$ [37, 38].

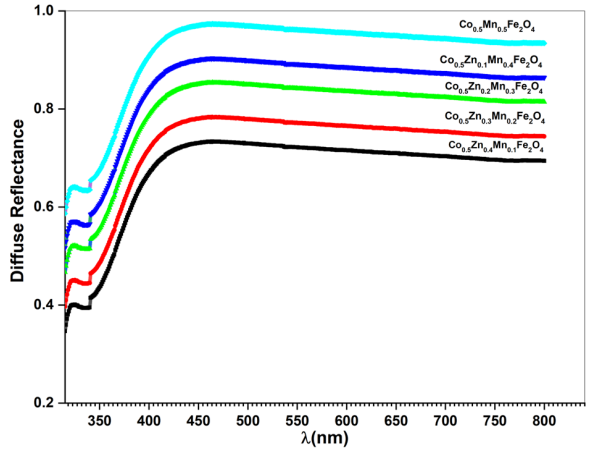

Figure 5. UV/Vis DRS spectra of the $Co_{0.5}Mn_{0.5-x}Zn_xFe_2O_4$ series.

The broad visible-light absorption is generally attributed to charge-transfer transitions from O^{2-} to Fe^{3+} ions, as well as d–d transitions of transition metal cations (Co^{2+}, Mn^{2+}, and Fe^{3+}) occupying tetrahedral (A) and octahedral (B) sites in the spinel lattice [38, 39]. With increasing Zn^{2+} content ($x = 0$–0.4), a systematic modification in both the absorption intensity and the edge position is observed. Zn^{2+} ions, having a filled $3d^{10}$ configuration, preferentially occupy tetrahedral (A) sites and do not directly contribute to d–d electronic transitions [39, 40]. Their incorporation induces redistribution of Fe^{3+} and other divalent cations between A and B sites to maintain charge balance [37, 39, 41]. This cation redistribution alters the Fe–O–Fe superexchange interactions, crystal field strength, and the overall electronic band structure [42]. Consequently, the optical absorption characteristics are modified, as reflected by changes in the slope and intensity of the DRS curves [43].

The variation in the absorption edge with Zn substitution indicates the tuning of the optical bandgap energy (E_g). In mixed spinel ferrites, Zn incorporation often leads to changes in E_g owing to the altered cation distribution and modified electronic interactions between the metal cations and oxygen anions [41, 44]. Depending on the degree of substitution and structural disorder, the band gap may either slightly increase owing to reduced Fe–O–Fe interactions or decrease owing to the introduction of defect states and localized energy levels within the band structure [45]. In nanoparticle systems, additional contributions from the surface states and possible quantum confinement effects may further influence the optical response [46, 47].

3.3. Determination of Optical Constant

The energy gap was calculated for $Co_{0.5}Mn_{0.5-x}Zn_xFe_2O_4$ NPs using Eq (7) and is presented in Figure (6) The indirect band gap of $Co_{0.5}Mn_{0.5-x}Zn_xFe_2O_4$ found to decrease from 2.96 to 2.81 eV (as shown in Table 2) with increasing Zn^{2+} ratios, which is related to the fact that the values of spinel ferrites vary significantly depending on the composition and doping. Studies on Co-Mn ferrites show band gaps in the range of approximately 3.8 to 4.3 eV [44, 48], with Mn doping generally increasing the band gap slightly. Zn doping in $CoFe^2O^4$ nanoparticles tends to slightly decrease the band gap, with values reported to be

around 3.06 to 3.15 eV. In contrast, Co-Zn ferrites with increasing Co content show a decrease in the band gap from approximately 2.5 to 3.1 eV, indicating that Co substitution narrows the band gap [49–51].

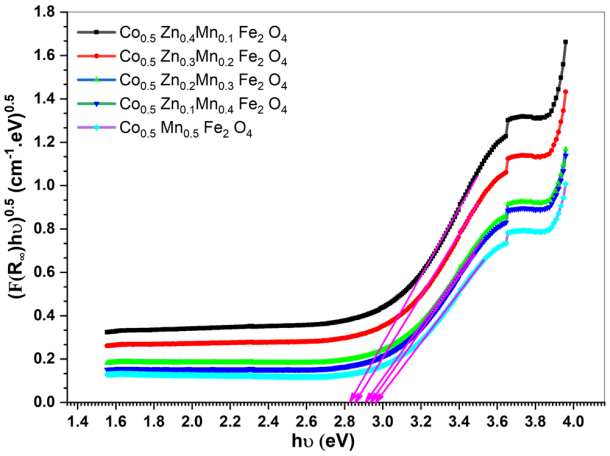

Figure 6. Curves for energy gap determination for the $Co_{0.5}Zn_{0.3}Mn_{0.2}Fe_2O_4$ nanocomposites.

Other studies on nanoferrite thin films have reported an indirect band gap near 1.2 eV, enhanced Co3d–O2p hybridization with Zn substitution, which raises the valence band maximum and narrows the indirect band gap [52, 53], and a direct gap at 2.7 eV [54, 55], suggesting complex electronic transitions depending on structure and measurement method. Overall, a band gap between (2.81 and 2.96 eV) for $Co_{0.5}Mn_{0.5-x}Zn_xFe_2O_4$ series is plausible as an intermediate value influenced by both Zn and Mn doping effects, consistent with trends showing Zn reduces and Mn increases the band gap relative to pure cobalt ferrite [55, 56]. This highlights the tunability of optical properties in these mixed-metal spinel ferrites through compositional control.

Figure (7) depicts the absorption coefficients of the prepared $Co_{0.5}Mn_{0.5-x}Zn_xFe_2O_4$ nanocomposites. The absorption coefficient α of $Co_{0.5}Mn_{0.5-x}Zn_xFe_2O_4$ nanocomposites depends on the wavelength owing to electron-photon interactions that influence optical losses through absorption and scattering. Similar studies on transition metal-doped ZnO films have revealed that doping levels and types significantly affect the absorption coefficient [57].

In addition, the absorption coefficients increased with the substitution ratio, increasing from x=0 to x=0.4 for Mn^{2+} cations by Zn^{2+} cations in the A-site of their $Co_{0.5}Mn_{0.5-x}Zn_xFe_2O_4$ spinal nanoferrites series.

Figure (8) depicts the variation of the extinction coefficient (k) with the photon energy for the prepared $Co_{0.5}Mn_{0.5-x}Zn_xFe_2O_4$ nanocomposite. The k values were estimated using $k = (\alpha\lambda/4\pi)$ [58]. From the figure, it can be observed that the k values increase with the substitution of Zn^{2+} cation concentration.

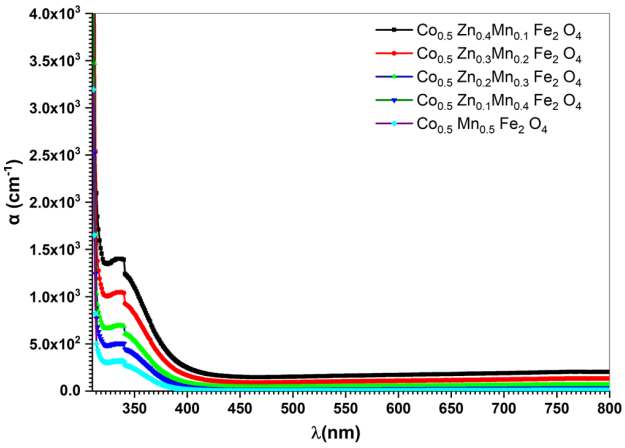

Figure 7. The variation between the absorption coefficient and wavelength of the $Co_{0.5}Mn_{0.5-x}Zn_xFe_2O_4$ samples.

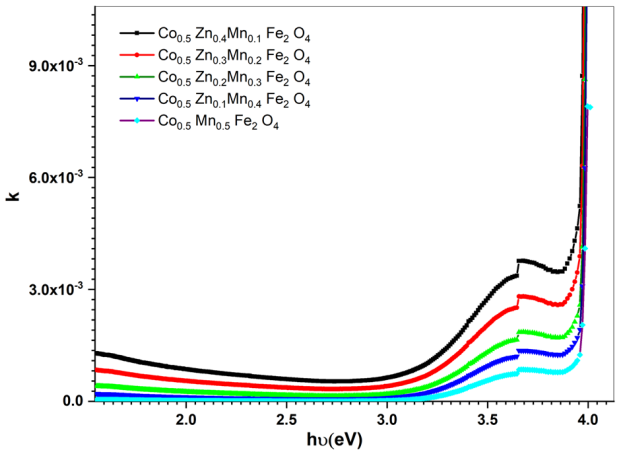

Figure 8. Variation of the extinction coefficient with photon energy for the prepared $Co_{0.5}Mn_{0.5-x}Zn_xFe_2O_4$ nanocomposites.

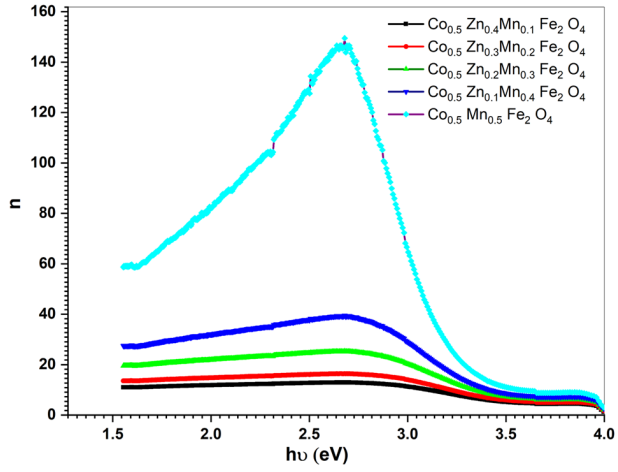

Figure 9. Variation of the refractive index with photon energy for the prepared $Co_{0.5}Mn_{0.5-x}Zn_xFe_2O_4$ nanocomposites.

The dependence of the refractive index on the photon energy is illustrated in Figure (9). The refractive index

is maximum for $Co_{0.5}Mn_{0.5}Fe_2O_4$ nanocomposites and decreases sequentially as the Zn^{2+} cation concentration increases from x=0 to x=0.4. The maximum value of n appears at hν =2.6 eV, where the maximum refractive index is observed near 2.6 eV (475 nm), which is independent of composition. In addition, this decreases in sequences, which aligns with observations in cobalt-doped ZnO thin films, where the refractive indices increase with Co content, reflecting changes in the electronic structure and defect states, according to the electron/photons interactions [59]. Because of these interactions, the refractive index noticeably changed with the variation in the wavelength of the incident light beam, that is, the absorption/scattering triggered an optical loss, which reduced the amplitudes of the transmission intensity oscillations at shorter wavelengths. Consequently, the extinction coefficient and refractive index with higher doping generally increase the absorption and refractive index values owing to enhanced density and polarization effects [60–62]. These optical parameters demonstrate the tunability of the optical response of Co-Zn-Mn ferrite nanoparticles through compositional control, which affects their potential applications in photonic devices and sensors [63, 64].

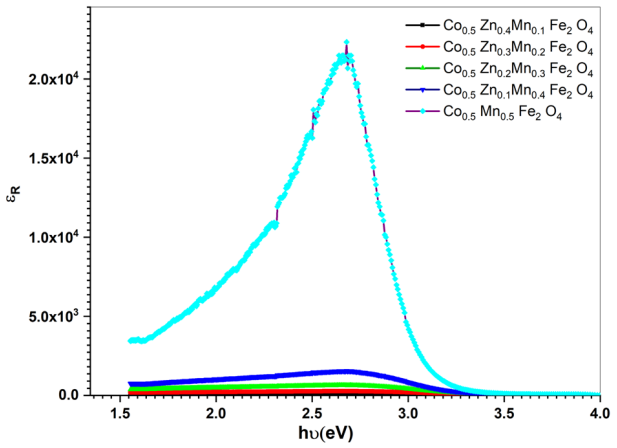

Figure 10. Variation of the real dielectric (ε_r) with photon energy for the prepared $Co_{0.5}Mn_{0.5-x}Zn_xFe_2O_4$ nanocomposites.

The variation in the real (ε_r) and imaginary (ε_i) parts of the dielectric constant as a function of the photon energy ($h\nu$) highlights the transition between high-energy electronic excitations and the transparent regime of the ferrite films. Figure (10) shows the variation in the real part of the dielectric constant (ε_r) with $h\nu$. It can be observed that ε_r follows the n behavior because the absorption (extinction coefficient, k) has minimal values in the visible spectrum, and the real dielectric part is dominated by the square of the refractive index. The decrease in ε_r with increasing $h\nu$ is a hallmark of normal dispersion, indicating that the electronic polarization response is most intense near the absorption edge (UV region) and gradually diminishes as the photon energy decreases. The highest value of ε_r decreased with decreasing Mn^{2+} cation ratios and increasing Zn^{2+} cation ratios.

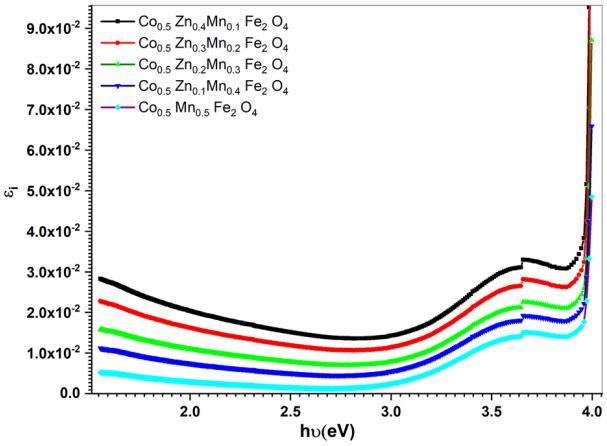

Figure 11. Variation of the imaginary dielectric constant (ε_i) with photon energy for the prepared $Co_{0.5}Mn_{0.5-x}Zn_xFe_2O_4$ nanocomposites.

The variation in the imaginary dielectric constant (ε_i) with hv is shown in Figure (11). It can be seen that the (ε_i) variation often follows the extinction coefficient„ which decreases in the $h\nu$=2.75 eV region; hence, the absorption for these photons is small in this region. This confirms that while the material maintains significant polarization owing to the presence of mixed-valence cations (such as Fe^{2+}/Fe^{3+} and Mn^{2+}/Mn^{3+}) in the spinel lattice, it does so with very little energy loss, making these films highly efficient for optoelectronic applications [2, 65, 66].

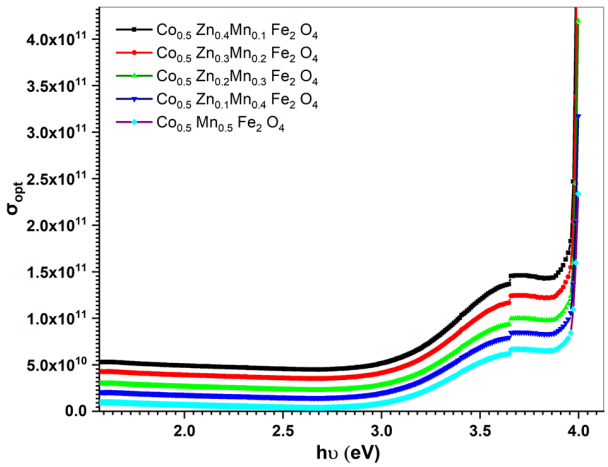

Figure 12. The dependence of optical conductivity (σ_{opt}) on the photon energy ($h\nu$) for the prepared $Co_{0.5}Mn_{0.5-x}Zn_xFe_2O_4$ nanocomposites.

The dependence of the optical conductivity (σ_{opt}) and electrical conductivity (σ_e) on the photon energy is pre-

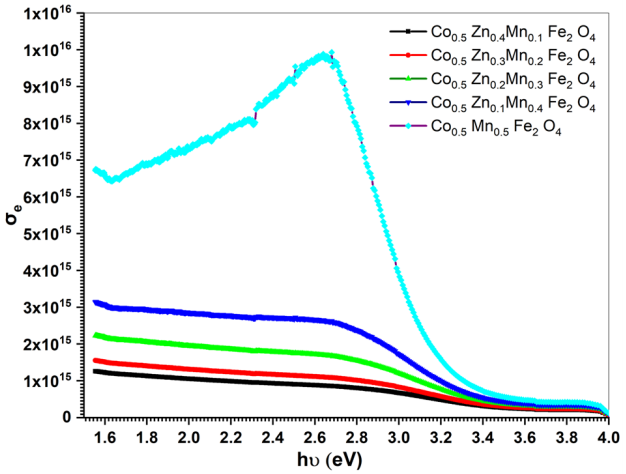

Figure 13. The dependence of electrical conductivity (σ_e) on the photon energy ($h\nu$) for the prepared $Co_{0.5}Mn_{0.5-x}Zn_xFe_2O_4$ nanocomposites.

sented in Figure (12) and (13), respectively. The observation of a high optical conductivity peak at 3.6 eV (344 nm) provides significant insight into the electronic transitions occurring within the spinel lattice of the $Co_{0.5}Mn_{0.5-x}Zn_xFe_2O_4$ material. This behavior is primarily attributed to the high density of states and the increased probability of interband transitions as the incident photon energy matches the fundamental bandgap of the nanoparticles. In this quaternary system, the presence of Mn^{2+} and Co^{2+} ions at the octahedral (B) sites facilitates multiple charge transfer mechanisms, such as $O^{2-} \rightarrow Fe^{3+}$ and $Fe^{3+} \leftrightarrow Fe^{2+}$ transitions [2, 67]. As the photon energy increases, the absorption coefficient (α) increases sharply, leading to a higher rate of electron-hole pair generation. The resulting increase in σ_{opt} can be mathematically understood through its dependence on the refractive index (n) and absorption coefficient (α) via the relation $\sigma_{opt} = \alpha nc/4\pi$ [64]. Furthermore, the correlation between the optical and electrical conductivities in the high-energy regime suggests that the photoexcited electrons contribute to a hopping conduction mechanism, where carriers move between the localized states of mixed-valence cations. This intense photo-response in the near-UV region effectively demonstrates that these nanoparticles are optimized for applications requiring efficient light-to-charge conversion, such as UV-shielding materials and high-sensitivity photodetectors [68, 69]. The optical conductivity and electrical conductivity σ_e of $Co_{0.5}Mn_{0.5-x}Zn_xFe_2O_4$ nanocomposites behavior revealed that the σ_{opt} increased with σ_e decreased as a function of Zn^{2+} in their nanoferrite material, for which the σ_{opt} increased while σ_e decreased with Zn^{2+} due to enhanced localization of charge carriers.

4. CONCLUSION

$Co_{0.5}Mn_{0.5-x}Zn_xFe_2O_4$ (x = 0 – 0.4) nanoferrites were successfully synthesized using the citrate–nitrate sol–gel auto-combustion method. XRD analysis confirmed the formation of a single-phase cubic spinel structure (Fd-3m) with a refined lattice parameter of a = 8.370 Å and high structural reliability (x^2 = 0.15). The crystallite size ranged between 8.017 and 10.130 nm, while the variation in dislocation density and microstrain indicated changes in lattice defects with Zn substitution. FTIR spectra showed characteristic metal–oxygen vibrations at 585 cm^{-1} and 415 cm^{-1}, corresponding to tetrahedral and octahedral sites of the spinel structure. UV–Vis DRS analysis revealed strong absorption in the UV–visible region with an optical band gap decreasing from 2.96 to 2.81 eV as Zn concentration increased, demonstrating tunable electronic properties. Optical constants indicated that the absorption coefficient, extinction coefficient, imaginary dielectric constant, and optical conductivity increased, while the refractive index and real dielectric constant decreased with increasing Zn content. The refractive index exhibited a maximum near 2.6 eV (475 nm), and a prominent optical conductivity peak appeared at 3.6 eV, attributed to interband transitions and charge transfer processes involving Fe^{2+}/Fe^{3+} ions. These findings confirm that Zn substitution effectively tailors the structural and optical properties of Co–Mn ferrites, making them promising materials for optoelectronic and photonic applications.

Acknowledgement: The Authors are grateful to the Material lab of Department of Physics, College of Science and Techniques, Alneelain University, Khartoum.

REFERENCES

[1] S. J. Salih and W. M. J. H. Mahmood, “Review on magnetic spinel ferrite (mfe2o4) nanoparticles: From synthesis to application,” vol. 9, no. 6, 2023.

[2] V. Singh, “An overview on recent trends of spinel ferrites (mfe2o4: M=fe2+, co2+, mn2+, ni2+, zn2+) synthesis and catalytic applications,” vol. 12, no. 3, pp. 283–317, 2025.

[3] T. Dippong, E. A. Levei, and O. Cadar, “Recent advances in synthesis and applications of mfe2o4 (m=co, cu, mn, ni, zn) nanoparticles,” vol. 11, no. 6, p. 1560, 2021.

[4] A. Rao, P. Thakur, and A. Thakur, “Future perspectives of spinel nano-ferrites,” in *Applications of Spinel Nano-Ferrites in Health, Environmental Sustainability, and Safety*, CRC Press, 2025, pp. 213–224.

[5] S. Kalia, R. Jasrotia, and V. P. Singh, *Magnetic Nanoferrites and Their Composites: Environmental and Biomedical Applications*. Elsevier, 2023.

[6] T. Mariam, “Magnetic characteristics of zinc substituted cobalt ferrites,” M.S. thesis, University of Dhaka, 2019.

[7] S. Mazen, N. Abu-Elsaad, and A. Nawara, “The influence of various divalent metal ions (mn2+, co2+, and cu2+) substitution on the structural and magnetic properties of nickel–zinc spinel ferrite,” *Phase Transitions*, vol. 62, no. 7, pp. 1183–1194, 2020.

[8] M. Dhiman, S. Bhukal, B. Chudasama, and S. Singhal, "Impact of metal ions (cr3+, co2+, ni2+, cu2+ and zn2+) substitution on the structural, magnetic and catalytic properties of substituted co–mn ferrites synthesized by sol–gel route," *J. Sol-Gel Sci. Technol.*, vol. 81, no. 3, pp. 831–843, 2017.

[9] S. Sushant, N. J. Choudhari, S. Patil, M. Rendale, S. Mathad, and A. Pathan, "Development of m–nife2o4 (co, mg, cu, zn, and rare earth materials) and the recent major applications," *Int. J. Sci. High Technol. Sci.*, vol. 32, no. 2, pp. 61–116, 2023.

[10] M. I. A. A. Maksoud et al., "Insights on magnetic spinel ferrites for targeted drug delivery and hyperthermia applications," vol. 11, no. 1, pp. 372–413, 2022.

[11] M. Almessiere et al., "Synthesis of dy-y co-substituted manganese-zinc spinel nanoferrites induced anti-bacterial and anti-cancer activities: Comparison between sonochemical and sol-gel auto-combustion methods," vol. 116, p. 111 186, 2020.

[12] M. S. A. Maashani, K. A. Khalaf, A. M. Gismelseed, and I. A. Al-Omari, "The structural and magnetic properties of the nano-cofe2o4 ferrite prepared by sol-gel auto-combustion technique," *J. Alloy. Compd.*, vol. 817, p. 152 786, 2020.

[13] N. A. Jasim, S. E. Ebrahim, and S. H. Ammar, "Photocatalytic degradation of rhodamine b utilizing core/shell structures (zn0.3mn0.7fe2o4@agvo3) under the irradiation of visible light," in *AIP Conference Proceedings*, vol. 3219, AIP Publishing, 2024, p. 020 062.

[14] L. Y. Gemachu and A. L. Birhanu, "Green synthesis of zno, cuo and nio nanoparticles using neem leaf extract and comparing their photocatalytic activity under solar irradiation," *Green Chem. Lett. Rev.*, vol. 17, no. 1, p. 2 293 841, 2024.

[15] R. A. Althobiti, M. Morsi, E. Alzahrani, and A. Al-Muntaser, "Enhancing the performance of pvc/pmma polymer blend through hybrid nanofiller of tio2 nps/gnps for capacitive energy storage applications," *Ceram. Int.*, vol. 50, no. 11, pp. 19 039–19 047, 2024.

[16] A. Al-Muntaser, M. Nasher, and M. Makhlouf, "Structural, electrical, and linear/nonlinear optical characteristics of thermally evaporated molybdenum oxide thin films," *Ceram. Int.*, vol. 48, no. 6, pp. 8069–8080, 2022.

[17] Y. A. Alsabah, M. S. AlSalhi, A. A. Elbadawi, and E. M. Mustafa, "Synthesis and study of the effect of ba2+ cations substitution with sr2+ cations on structural and optical properties of ba2xsrxznwo6 double perovskite oxides," *Materials*, vol. 10, no. 5, p. 469, 2017.

[18] E. M. A. Nassar, A. AL-Hammadi, and Y. H. I. Mohammed, "Morphological and optical analysis of -al2o3:zn nanoparticles," *Sana'a Univ. J. Appl. Sci. Technol.*, vol. 3, no. 6, pp. 1408–1418, 2025.

[19] F. Chen, C. Niu, Q. Yang, X. Li, and G. Zeng, "Facile synthesis of visible-light-active bioi modified bi2moo6 photocatalysts with highly enhanced photocatalytic activity," *Ceram. Int.*, vol. 42, no. 2, pp. 2515–2525, 2016.

[20] C. Lan, S. Zhao, T. Xu, J. Ma, S. Hayase, and T. Ma, "Investigation on structures, band gaps, and electronic structures of lead free la2nimno6 double perovskite materials for potential application of solar cell," *J. Alloy. Compd.*, vol. 655, pp. 208–214, 2016.

[21] A. Al-Muntaser, R. A. Pashameah, E. Alzahrani, S. A. Al-Subhi, and A. Tarabiah, "Tuning structural, optical, and dispersion functions of polystyrene via addition of meso-tetraphenylporphine manganese (iii) chloride towards optoelectronic applications," *Opt. Mater.*, vol. 135, p. 113 333, 2023.

[22] A. Alosabi, A. Al-Muntaser, M. El-Nahass, and A. Oraby, "Effect of heat treatment on structure, surface morphology, linear and nonlinear optical properties of na2pc films for optoelectronic applications," *Opt. & Laser Technol.*, vol. 158, p. 108 846, 2023.

[23] A. A. Al-Muntaser et al., "Enhanced linear and nonlinear optical properties of poly (vinyl alcohol) films with manganese (iii) tetraphenylporphyrin chloride additive for optoelectronic applications," *Polym. Int.*, vol. 75, no. 4, pp. 298–308, 2026.

[24] M. F. Al-Mudhaffer, M. A. Nattiq, and M. A. Jaber, "Linear optical properties and energy loss function of novolac: Epoxy blend film," *Arch. Appl. Sci. Res.*, vol. 4, no. 4, pp. 1731–1740, 2012.

[25] D. D. Andhare, S. R. Patade, S. A. Jadhav, S. B. Somvanshi, and K. Jadhav, "Rietveld refined structural, morphological, raman and magnetic investigations of superparamagnetic zn–co nanospinel ferrites prepared by cost-effective co-precipitation route," *Appl. Phys. A*, vol. 127, no. 6, p. 480, 2021.

[26] P. Saha, S. K. Shil, P. Roy, R. S. Auntu, N. I. Khan, and S. Sikder, "Exploring the structural, magnetic, dielectric and electrical properties of solid state method synthesized mn3+ substituted co–zn ferrites," *J. Mater. Sci.*, vol. 60, no. 37, pp. 17 051–17 064, 2025.

[27] S. Talebniya, I. Sharifi, M. Saeri, and A. Doostmohammadi, "Study of cation distribution and magnetic properties of mfe2o4 (m=fe, co, zn, mn, and cu) nanoparticles," *J. Supercond. Nov. Magn.*, vol. 35, no. 3, pp. 899–908, 2022.

[28] R.-G. Ciocarlan et al., "In-depth structural characterization and magnetic properties of quaternary ferrite systems co0.5zn0.25m0.25fe2o4 (m=ni, cu, mn, mg)," *J. Alloy. Compd.*, vol. 816, p. 152 674, 2020.

[29] A. Kamzin et al., "Structure and properties of coxmn1xfe2o4 nanoparticles depending on the amount of co ions (0x1.0)," vol. 64, no. 6, 2022.

[30] G. Datt and A. Abhyankar, "Dopant driven tunability of dielectric relaxation in mxco(1-x)fe2o4 (m: Zn2+, mn2+, ni2+) nano-ferrites," *J. Appl. Phys.*, vol. 122, no. 3, 2017.

[31] B. Ghalib and M. Hessien, "Magnetic and antibacterial properties of substituted cobalt spinel ferrite nanocomposites synthesized via henna green microwave hydrothermal method," *Sci. Reports*, vol. 15, no. 1, p. 16 653, 2025.

[32] P. Pankaew, P. Nawarat, and J. Chokboribal, "Fabrication and characterization of biodegradable zn-ni spinel ferrite/-tcp composite ceramics exhibiting enhanced cell colonization," *J. Mater. Sci. Mater. Med.*, vol. 37, no. 1, p. 31, 2026.

[33] P. Banshiwal et al., "Impact of cu-substitution on the dielectric properties and electronic structure of cobalt nanoferrites," vol. 86, no. 10, pp. 969–980, 2025.

[34] W. Anukool, R. A. El-Nabulsi, and S. Dabagh, "Effect of al3+ doping on dielectric properties of cobalt ferrite nanoparticle for using in high frequency applications," *J. Sol-Gel Sci. Technol.*, vol. 105, no. 2, pp. 405–415, 2023.

[35] P. Punia et al., "Microstructural, optical and magnetic study of ni–zn nanoferrites," vol. 34, no. 8, pp. 2131–2140, 2021.

[36] H. Mahajan, S. K. Godara, and A. Srivastava, "Synthesis and investigation of structural, morphological, and magnetic properties of the manganese doped cobalt-zinc spinel ferrite," *J. Alloy. Compd.*, vol. 896, p. 162 966, 2022.

[37] R. Waldron, "Infrared spectra of ferrites," *Phys. Rev.*, vol. 99, no. 6, p. 1727, 1955.

[38] W. Fontijn, P. V. der Zaag, L. Feiner, R. Metselaar, and M. Devillers, "A consistent interpretation of the magneto-optical spectra of spinel type ferrites," *J. Appl. Phys.*, vol. 85, no. 8, pp. 5100–5105, 1999.

[39] A. Moskvin and R. Pisarev, "Optical spectroscopy of charge transfer transitions in multiferroic manganites, ferrites, and related insulators," *Low Temp. Phys.*, vol. 36, no. 6, pp. 489–510, 2010.

[40] Z. Jia, D. Ren, Q. Wang, L. Xu, and R. Zhu, "Structural and magnetic properties of co1xznxfe2o4 nanorods prepared by the solvothermal annealing method," *Ceram. Int.*, vol. 39, no. 6, pp. 6113–6118, 2013.

[41] A. A. Ati, A. H. Abdalsalam, and A. S. Hasan, "Thermal, microstructural and magnetic properties of manganese substitution cobalt ferrite prepared via co-precipitation method," *J. Mater. Sci. Mater. Electron.*, vol. 32, no. 3, pp. 3019–3037, 2021.

[42] M. Almessiere et al., "Effect of nb substitution on magneto-optical properties of co0.5mn0.5fe2o4 nanoparticles," vol. 1195, pp. 269–279, 2019.

[43] T. Zeeshan, S. Anjum, S. Waseem, F. Majid, M. D. Ali, and A. Aslam, "Influence of zinc substitution on structural, elastic, magnetic and optical properties of cobalt chromium ferrites," *Mater. Sci.*, vol. 39, no. 1, pp. 139–151, 2021.

[44] S. Ansari, D. Phase, Y. Kolekar, and C. Ramana, "Effect of manganese-doping on the chemical and optical properties of cobalt ferrite nanoparticles," *Mater. Sci. Eng. B*, vol. 300, p. 117 134, 2024.

[45] L. Xue et al., "Study of electron transition energies between anions and cations in spinel ferrites using differential uv–vis absorption spectra," vol. 492, pp. 61–64, 2016.

[46] J. M. Sulaiman, M. M. Ismail, S. N. Rafeeq, and A. Mandal, "Enhancement of electromagnetic interference shielding based on co0.5zn0.5fe2o4/pani-ptsa nanocomposites," *Appl. Phys. A*, vol. 126, no. 3, p. 236, 2020.

[47] M. A. Bashar et al., "Hydrothermal synthesis of cobalt substitute zinc-ferrite (co1-xznxfe2o4) nanodot, functionalised by polyaniline with enhanced photocatalytic activity under visible light irradiation," vol. 9, no. 4, 2023.

[48] H. Etemadi and P. G. Plieger, "Improvements in the organic-phase hydrothermal synthesis of monodisperse mxfe3xo4 (m=fe, mg, zn) spinel nanoferrites for magnetic fluid hyperthermia application," *ACS Omega*, vol. 5, no. 29, pp. 18 091–18 104, 2020.

[49] M. Jamil et al., "Effect on structural and optical properties of zn-substituted cobalt ferrite cofe2o4," vol. 13, no. 1, pp. 45–53, 2017.

[50] M. N. Nawaz, U. Ghazanfar, W. Yuan, H. Wahab, O. T. Satti, and S. B. Khan, "Impact of cobalt doping on the properties of zinc ferrite (coxzn1-xfe2o4)," *J. Mater. Sci. Mater. Electron.*, vol. 36, no. 13, p. 790, 2025.

[51] M. N. Akhtar, M. S. Nazir, Z. Tahir, S. Qamar, and M. A. Khan, "Impact of co doping on physical, structural, microstructural and magnetic features of mgzn nanoferrites for high frequency applications," *Ceram. Int.*, vol. 46, no. 2, pp. 1750–1759, 2020.

[52] J. Kangsabanik, M. K. Svendsen, A. Taghizadeh, A. Crovetto, and K. S. Thygesen, "Indirect band gap semiconductors for thin-film photovoltaics: High-throughput calculation of phonon-assisted absorption," *J. Am. Chem. Soc.*, vol. 144, no. 43, pp. 19 872–19 883, 2022.

[53] S. Chavan, M. Babrekar, S. More, and K. Jadhav, "Structural and optical properties of nanocrystalline ni–zn ferrite thin films," *J. Alloy. Compd.*, vol. 507, no. 1, pp. 21–25, 2010.

[54] I. Hernandez-Calderon, "Optical properties and electronic structure of wide band gap ii-vi semiconductors," in *II-VI Semiconductor Materials and Their Applications*, Routledge, 2018, pp. 113–170.

[55] B. Holinsworth et al., "Chemical tuning of the optical band gap in spinel ferrites: Cofe2o4 vs nife2o4," vol. 103, no. 8, 2013.

[56] C. Himcinschi et al., "Optical and magneto-optical study of nickel and cobalt ferrite epitaxial thin films and submicron structures," vol. 113, no. 8, 2013.

[57] A. Parveen et al., "Microstructural, optical, dielectric, and magnetic properties of multifunctional zn1-xfexo nanoparticles," pp. 1–13, 2024.

[58] A. Al-Muntaser et al., "Enhancement of the structural, optical, and dispersion performance of polyvinyl alcohol via coronene additive for optoelectronic applications," *Phys. Scripta*, vol. 98, no. 11, p. 115 964, 2023.

[59] E. B. Buzok, S. Yalcin, G. Demircan, D. Yılmaz, B. Aktaş, and E. Aytar, "Effect of a cobalt complex on the structural, optical, electrical, and anti-reflective properties of zno thin films," *Ceram. Int.*, 2025.

[60] A. Henaish et al., "Synthesize, characterization, dielectric, linear and nonlinear optical properties of ni–al ferrite/pani nanocomposite film," vol. 119, p. 111 397, 2021.

[61] M. N. Akhtar, "Gd doped cu-ni-zn nano ferrite absorbers for broadband microwave absorption: Physicochemical, electromagnetic, and reflection loss evaluations," *Ceram. Int.*, vol. 51, no. 9, pp. 12 262–12 272, 2025.

[62] I. A. Salmani, T. Murtaza, M. S. Khan, and M. S. Khan, "Analysis of size-dependent variation in nonlinear absorption coefficient of multiferroic bismuth ferrite nanoparticles synthesized at different sintering temperature," *J. Nanosci. Optoelectron.*, vol. 31, no. 03, p. 2 250 012, 2022.

[63] T. Dippong, O. Cadar, F. Goga, D. Toloman, and E. A. Levei, "Impact of ni content on the structure and sonophotocatalytic activity of ni-zn-co ferrite nanoparticles," *Int. J. Mol. Sci.*, vol. 23, no. 22, p. 14 167, 2022.

[64] A. Al-Muntaser, E. Alzahrani, A. F. A. Naim, R. Alwafi, and A. Saeed, "Linear and nonlinear optical properties of pvc/pmma polymer blends reinforced with tio2/gnp hybrid fillers for optoelectronics applications," *Phys. Scripta*, vol. 100, no. 8, p. 085 904, 2025.

[65] S. Agrohiya et al., "Fabrication of znmn2o4 spinel thin film devices for solar-blind ultraviolet photodetectors: Effect of zn2+ concentration," vol. 34, no. 6, p. 514, 2023.

[66] M. Sharma, K. Bera, R. Mishra, and A. V. Kuanr, "Structural, magnetic, and optical properties of mn2+ doping in zno thin films," *SN Appl. Sci.*, vol. 4, no. 4, pp. 268–278, 2021.

[67] M. Khalif et al., "Adsorption of o2 molecule on the transition metals tm(ii) porphyrins induced carbon nanocone," vol. 119, p. 108 362, 2023.

[68] N. Hadia et al., "Decoding the structure–property paradigm in lix5sb11 (x=fe, mn) skutterudites: A synergistic computational–experimental exploration," pp. 1–19, 2026.

[69] A. Mansour, M. Morsy, A. M. E. Nahrawy, and A. B. A. Hammad, "Humidity sensing using zn(1.6x)na0.4cuxtio4 spinel nanostructures," *Sci. Reports*, vol. 14, no. 1, p. 562, 2024.